

Evolving dunes under flow reversals: from an initial heap toward an inverted dune

W. R. Assis¹, E. M. Franklin¹, N. M. Vriend^{2,3,4,5}

¹School of Mechanical Engineering, UNICAMP - University of Campinas, Rua Mendeleev, 200,
Campinas, SP, Brazil

²BP Institute, University of Cambridge, Cambridge, UK

³Department of Applied Mathematics and Theoretical Physics, University of Cambridge, Cambridge, UK

⁴Department of Earth Sciences, University of Cambridge, Cambridge, UK

⁵Current address: Department of Mechanical Engineering, University of Colorado Boulder, Boulder, USA

Key Points:

- Experiments show that 2D dunes grow and develop over a characteristic time that matches that of fully 3D barchan dunes
- The morphodynamics of reversing dunes over time are revealed by fully reversing the flow direction and tracking the rebuilding and reshaping
- Numerical simulations on a reversing 3D barchan show that its central slice behaves as the reversing 2D dunes

Corresponding author: Willian Assis, righiassis@gmail.com

Abstract

Sand dunes are ubiquitous in nature, and are found in abundance on Earth and other planetary environments. One of the most common types are crescent-shaped dunes known as barchans, whose mid-line could be assumed to behave as 2D dunes. In this work, we (i) compare the morphology of the mid-line of 3D barchans with 2D dunes; and (ii) track the evolution of 3D barchan and 2D dunes under bi-modal changes in the flow direction. We performed experiments in a 2D flume on 2D dunes and Euler-Lagrange simulations of 3D bedforms. The reversal experiments start with an initial heap deforming into a steady-state dune, which is then perturbed by reversing the flow, resulting in an inverted dune. We show that during the reversal the grains on the lee side immediately climb back onto the dune while its internal part and toe remain static, forming a new lee face on the previous stoss slope of varying angle. We determine that (i) the characteristic time for the development of 2D dunes scales identically with that for 3D barchans, (ii) that the time for dune reversal is twice the time necessary to develop an initial heap to steady-state, and (iii) that a considerable part of grains remain static during the entire process. Our findings reveal the mechanisms for dune reversal, and highlight that numerical computations of 2D barchans, which are more feasible in geophysical scales, predict realistic outcomes for the relevant time-scales.

Plain Language Summary

Crescent-shaped dunes, known as barchans, are found in abundance on Earth and other planetary environments. Although their different shapes and manifestations intrigue us and produce fascinating images, the underlying physics still challenges us. Here we investigate two critical questions: (i) can we capture all relevant physical processes of 3D dunes in a 2D slice? and (ii) how does the dune morph over space and time upon flow reversal (e.g. the wind blowing from the opposite direction)? We research these questions by carrying out experiments with 2D dunes in a water flume and numerical simulations of 3D barchans, and flip-around our flow forcing to investigate flow reversal. We find that the typical development times for 2D and 3D dunes are equivalent and reveal details of the rebuilding processes of the dune upon flow reversals. Interestingly, the inversion time after flow reversal is twice that of the formation time of the initial heap, and a considerable part of grains remains static during the entire process. Our findings reveal the mechanisms for dune reversal and show that 2D simulations, which are simpler and faster, reproduce the underlying physics.

1 Introduction

Sand dunes are bedforms resulting from erosion and deposition of sand by the action of a fluid flow (Bagnold, 1941; Hersen et al., 2002), and they are frequently found on Earth, Mars and other celestial bodies (Hersen, 2004; Elbelrhiti et al., 2005; Claudin & Andreotti, 2006; Parteli & Herrmann, 2007; Courrech du Pont, 2015). Among the most common are crescent-shaped dunes, known as barchans, that appear under an one-directional flow regime and when the quantity of available sand is limited.

Given the abundance of barchans present in nature, a considerable number of field measurements, experiments, and numerical simulations were conducted over the last decades (C. Sauermaun et al., 2000; Hersen et al., 2002; Andreotti et al., 2002; Hersen et al., 2004; Hersen, 2004; Kroy et al., 2005, 2002b; Parteli et al., 2007; Andreotti et al., 2009; Franklin & Charru, 2011; Pähtz et al., 2013; Kidanemariam & Uhlmann, 2014; Guignier et al., 2013; Parteli et al., 2011; Khosronejad & Sotiropoulos, 2017), but only very few of them were carried out at the grain scale (Alvarez & Franklin, 2018, 2019, 2020, 2021; Assis & Franklin, 2020, 2021). Most analytical models and numerical simulations are based on information from field measurements on aeolian dunes, so that they solve the problem at the bedform scale only by considering that the grains move mainly in the longitudinal direction (typical of aeolian saltation). For example, the first numerical simulations considered the granular system as a continuum medium, some of them modeling 3D dunes as vertical slices that behave as 2D dunes. Those models hypothesize that grains move in the longitudinal direction, while transverse diffusion transfers a small quantity of mass between adjoining slices (G. Sauermaun et al., 2001; Herrmann & Sauermaun, 2000; Kroy et al., 2002a, 2002b, 2005; Schwämmle & Herrmann, 2005; Parteli et al., 2014). Therefore, the continuum-sliced models are, in principle, valid for aeolian barchans, which consist of a large number of grains that are entrained mainly in longitudinal direction, with small lateral motion (due to reptation). However, this is not necessarily the case of subaqueous barchans where transverse sediment transport can become dominant.

Some recent works showed that the transverse motion of grains is important for subaqueous barchans (Alvarez & Franklin, 2018, 2019), indicating that the picture of a 3D dune as connected slices must be refined in the subaqueous case. For instance, Alvarez and Franklin (2018, 2019) measured experimentally the displacement of individual grains migrating to horns as an initial pile was deformed into a barchan dune. They found that most of those grains come from upstream regions on the periphery of the dune, within angles forming 105° and 160° and 210° and 260° in the flow direction (0° pointing downstream). Those results were later corroborated by numerical simulations at the grain scale using large eddy simulation coupled with discrete element method (LES-DEM, Alvarez & Franklin, 2020, 2021; Lima et al., 2022). In this picture, grains migrating to horns have considerable transverse displacements (of the order of the dune size), contradicting, for subaqueous barchans, the models based on connected slices. Note however that the results show that grains going to horns do not come from the dune centerline.

Based on discrete simulations using a cellular automaton model, Zhang et al. (2014) found that the residence time of grains within a barchan dune, in particular in the central slice, is relatively large, being of the order of many turnover times of the barchan. They showed that the large residence time occurs because of a cyclic process: grains on the stoss side tend to disperse toward the laterals (as also shown by the experiments of Assis & Franklin, 2021), but are returned to the central region after avalanching on the lee side due to the curvature of the barchan dune. On the whole, Zhang et al. (2014) showed that transverse mixing in the central slice is restricted by this dispersion-concentration mechanism, and proposed that the central slice contains most of the information (and memory) of the barchan morphodynamics. This result is not, in principle, in contradiction with those of Alvarez and Franklin (2018, 2019), since the latter found that grains populating the horns (and afterward leaving the barchan) do not come from the central slice.

103 Because the interior (e.g, the central slice) of real dunes is not accessible in exper-
 104 iments, Bacik et al. (2020); Bacik, Caulfield, and Vriend (2021); Bacik, Canizares, et al.
 105 (2021) carried out experiments with 2D dunes in a narrow Couette-type circular water
 106 flume. Bacik et al. (2020) investigated how 2D dunes interact with each other under a
 107 turbulent water flow, and found that the turbulent structures of the flow trigger a long
 108 range dune-dune repulsion (preventing dune-dune collisions). Later Bacik, Caulfield, and
 109 Vriend (2021), inquired into the stability of a pair of dunes and proposed a parameter
 110 space where dune-dune interactions either stabilize or destabilize the initial configura-
 111 tion, and Bacik, Canizares, et al. (2021) showed how the presence of obstacles change
 112 the dune morphodynamics. If these findings can be proven valid for barchan dunes, they
 113 would represent a large advance toward understanding barchan fields.

114 Our aim is to investigate whether subaqueous 3D barchan dunes can be represented
 115 as connected slices, in essence as the 2D dune as introduced in Bacik et al. (2020); Bacik,
 116 Caulfield, and Vriend (2021); Bacik, Canizares, et al. (2021), or whether indeed the trans-
 117 verse sediment transport radically changes the physical behavior and needs to be accounted
 118 for. In addition, we are investigating whether the underlying physical processes of dune
 119 reversal leading to an inverted dune can be captured as a solely 2D process mimicking
 120 the mid-line of a 3D barchan dune. We are performing experiments in the 2D flume on
 121 heaps and reversing dunes and complement these experiments with numerical simula-
 122 tions at the grain-scale, which allows us to analyze the central slice of 3D dunes. In our
 123 numerical simulations, we apply the same forcing procedure as in our experiments: (1)
 124 pile formation, (2) development to a steady-state dune, (3) flow reversal and (4) equi-
 125 librating to a steady-state (reversed) dune. As the grains climb back up the lee side dur-
 126 ing the flow reversal stage, the internal part and the toe of the dune remain static while
 127 a new lee face with varying angle and length is formed on the former stoss slope. In this
 128 manuscript, we will identify characteristic times and scales of this reversal process, and
 129 identify the areas where the grains are remobilized in this re-morphing process. Our find-
 130 ings reveal the mechanisms for dune reversal and provide a validation between exper-
 131 imental data and numerical simulations.

132 2 Experimental Setup

133 The experimental setup is the same as used in Jarvis et al. (2022); Bacik et al. (2020),
 134 and consists of a periodic channel, a driving device, and an imaging system. The peri-
 135 odic channel is a circular flume with external and internal radii of 97 cm and 88 cm, re-
 136 spectively, filled to a level of 45.5 cm with water and particles, with parameters spec-
 137 ified in the next paragraph. A rotating rig with 12 equidistant paddles submerged near
 138 the water surface is mounted above the flume, providing a shearing motion to the wa-
 139 ter, while the flume is connected to a counter-rotating turntable. Our tests begin by im-
 140 posing a paddle rotation in the counter-clockwise direction (view from above) and a turntable
 141 rotation in the clockwise direction (we call this flow 0°). After reaching a steady-state
 142 developed dune, we revert both the paddle and turntable directions in order to obtain
 143 a reverse flow (180°). Figures 1a and 1b show a photograph and the layout of the ex-
 144 perimental setup, respectively.

145 We used round glass spheres ($\rho_s = 2500 \text{ kg/m}^3$, approximately), sieved to a diam-
 146 eter between $1.0 \text{ mm} \leq d \leq 1.3 \text{ mm}$, for which we consider the mean value as being \bar{d}
 147 $= 1.15 \text{ mm}$, and varied the total mass of the initial pile between 1 and 2 kg (see the sup-
 148 porting information for a photograph of the used particles). The flow direction was ei-
 149 ther 0° (initial flow) or 180° (reverse flow), and the water velocity varied within 0.81 m/s
 150 $\leq U \leq 1.22 \text{ m/s}$. In here, the relative velocity between the table and paddles is $U = R(\Omega_p -$
 151 $\Omega_t)$, the outer radius is $R = 97 \text{ cm}$, and Ω_p and Ω_t are the angular velocities of the pad-
 152 dles and table, respectively. The shear velocity u_* is computed based on Equation 8 of
 153 Jarvis et al. (2022), and was found to vary between $0.050 \text{ m/s} \leq u_* \leq 0.103 \text{ m/s}$. The
 154 Reynolds number $Re = Uw/\nu$ varied within 0.73×10^5 and 1.10×10^5 , where $w = 9$

155 cm is the width of the channel and ν the kinematic viscosity of water. The paddle and
 156 water heights were fixed for all tests, being 34.5 and 45.5 cm, respectively. Table 1 sum-
 157 marizes the test conditions, and images from experiments are available in an open reposi-
 158 tory (Assis et al., 2023). For a given velocity U , the exact angular velocities Ω_p and Ω_t
 159 were chosen empirically to reduce secondary flows in order to produce 2D dunes as sym-
 160 metrical as possible (lateral-view images from 2D dunes are available in the supporting
 161 information).

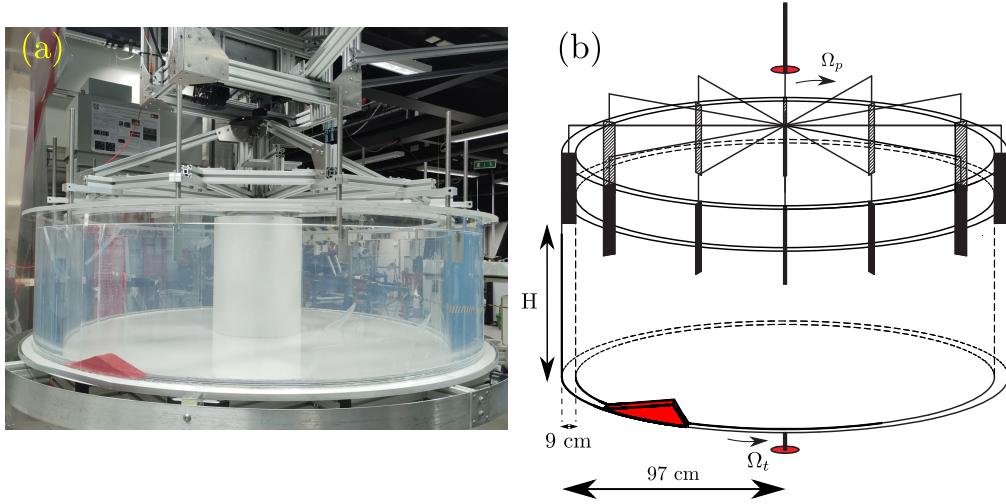


Figure 1. (a) Photograph and (b) Layout of the circular flume.

Case ...	Dune mass kg	Ω_p rpm	Ω_t rpm	$\Omega_p - \Omega_t$ rpm	Re ...	Flow direction degrees
<i>a</i>	2	4.60	-3.40	8	0.73×10^5	0
<i>b</i>	2	5.80	-4.20	10	0.91×10^5	0
<i>c</i>	2	7.00	-5.00	12	1.10×10^5	0
<i>d</i>	1	4.60	-3.40	8	0.73×10^5	0
<i>e</i>	1	5.65	-4.35	10	0.91×10^5	0
<i>f</i>	1	6.85	-5.15	12	1.10×10^5	0
<i>g</i>	2	-4.60	3.40	-8	0.73×10^5	180
<i>h</i>	2	-5.80	4.20	-10	0.91×10^5	180
<i>i</i>	2	-7.00	5.00	-12	1.10×10^5	180
<i>j</i>	1	-4.60	3.40	-8	0.73×10^5	180
<i>k</i>	1	-5.65	4.35	-10	0.91×10^5	180
<i>l</i>	1	-6.85	5.15	-12	1.10×10^5	180

Table 1. Label of tested cases, dune mass, angular velocity of paddles, angular velocity of the table, total angular velocity, channel Reynolds number Re , and flow orientation.

162 A camera of complementary metal-oxide-semiconductor (CMOS) type was mounted
 163 with a lateral view (i.e., in the radial direction) of the flume. We used a ISVI black and
 164 white camera, capable of acquiring images at a maximum resolution of 12MP at 181 Hz
 165 (model IC-X12S-CXP), and a Nikon lens of 60 mm focal distance and F2.8 maximum

166 aperture (model AF Micro Nikkor). In the experiments, we set the camera to operate
 167 with a region of interest (ROI) of 64 px \times 1,024 px at a frequency of 200 Hz. The field
 168 of view was 6.6 mm \times 105.5 mm, corresponding to a resolution of 9.7 px/mm. A col-
 169 umn in the central axis of the rotating experiment (see Figure 1) was illuminated with
 170 lamps of light-emitting diode (LED), enabling a good contrast between the sediment lay-
 171 ers and walls. The acquired images were afterward processed by numerical scripts that
 172 identify and reconstruct 2D profiles providing a dune shape.

173 3 Numerical Setup

174 We carried out numerical simulations using CFD-DEM (computational fluid dy-
 175 namics - discrete element method), in which we computed the formation of single barchans
 176 from initially conical piles and, after reaching a developed barchan shape, reversed the
 177 flow direction. Our simulations were performed at the grain scale by making use of LES
 178 (large eddy simulation) for CFD, which thus computed the mass (Equation 1) and mo-
 179 mentum (Equation 2) equations for the fluid using meshes of the order of the grains' di-
 180 ameter,

$$\nabla \cdot \vec{u}_f = 0, \quad (1)$$

$$\frac{\partial \rho_f \vec{u}_f}{\partial t} + \nabla \cdot (\rho_f \vec{u}_f \vec{u}_f) = -\nabla P + \nabla \cdot \vec{\tau} + \rho_f \vec{g} - \vec{f}_{fp}, \quad (2)$$

181 where \vec{g} is the acceleration of gravity, \vec{u}_f is the fluid velocity, ρ_f is the fluid density, P
 182 the fluid pressure, $\vec{\tau}$ the deviatoric stress tensor of the fluid, and \vec{f}_{fp} is the resultant of
 183 fluid forces acting on each grain by unit of fluid volume. The DEM solved the linear (Equa-
 184 tion 3) and angular (Equation 4) momentum equations applied to each solid particle,

$$m_p \frac{d\vec{u}_p}{dt} = \vec{F}_p, \quad (3)$$

$$I_p \frac{d\vec{\omega}_p}{dt} = \vec{T}_c, \quad (4)$$

185 where, for each grain, m_p is the mass, \vec{u}_p is the velocity, I_p is the moment of inertia, $\vec{\omega}_p$
 186 is the angular velocity, \vec{T}_c is the resultant of contact torques between solids, and \vec{F}_p is
 187 the resultant force (weight, contact and fluid forces). We made use of the open-source
 188 code CFDEM (Goniva et al., 2012) (www.cfdem.com), which couples the open-source
 189 CFD code OpenFOAM with the open-source DEM code LIGGGHTS (Kloss & Goniva,
 190 2010; Berger et al., 2015). A complete description of the fundamental and implemented
 191 equations, CFD meshes and convergence, DEM parameters, and tests can be found in
 192 Lima et al. (2022).

193 The CFD domain is a 3D channel of size $L_x = 0.4$ m, $L_y = \delta = 0.025$ m and L_z
 194 $= 0.1$ m, where x , y and z are the longitudinal, vertical and spanwise directions, respec-
 195 tively, with periodic conditions in the longitudinal and spanwise directions. The verti-
 196 cal dimension of the domain, $L_y = \delta$, corresponds to the channel half height (the real
 197 channel height being 2δ), and the height of smallest meshes (close to the bottom bound-
 198 ary) was $\Delta y = 2.9 \times 10^{-4}$ m, which corresponds to $\Delta y/d = 1.46$ (the values of d used
 199 in the simulations are shown next). The fluid is water, flowing with a cross-sectional mean
 200 velocity $U = 0.28$ m/s. The channel Reynolds number based on U , $\text{Re} = U2\delta\nu^{-1}$, is 14,000,
 201 and the Reynolds number based on shear velocity u_* , $\text{Re}_* = u_*\delta\nu^{-1}$, is 400, where ν is
 202 the kinematic viscosity (10^{-6} m²/s for water). The granular material consisted of 10^5
 203 glass spheres randomly distributed, with sizes following a Gaussian distribution within

204 0.15 mm $\leq d \leq$ 0.25 mm. The coefficients of sliding friction μ , rolling friction μ_r and
 205 restitution e , as well as the values of Poisson ratio σ , Young’s modulus E and density
 206 ρ_p used in the simulations are shown in Table 2 (extensive tests of these parameters are
 207 presented in Lima et al., 2022). We selected for the particles a solid wall boundary condi-
 208 tion at the bottom boundary, and a free exit at the outlet. Note that no influx of grains
 209 was imposed, so that the bedform lose grains and decrease slightly in size along time.
 210 We note also that the numerical setup differs from the experimental one in terms of fluid
 211 flow, grain diameter, boundary conditions, and size of the system. While, on the one hand,
 212 to simulate barchans with a size comparable to the 2D experiments would be compu-
 213 tationally unfeasible, on the other hand the numerical setup used has been extensively
 214 investigated and validated against experiments (Lima et al., 2022). In addition, the use
 215 of periodic conditions for the grains (to be closer to the experimental setup) would im-
 216 ply that grains leaving the two horns would return and reach regions close to the flanks
 217 of the barchan dune, deforming it considerably. More details about the equations, pa-
 218 rameters and meshes used in the simulations can be found in Lima et al. (2022).

Table 2. Physical properties of DEM particles.

DEM properties	
Sliding Friction Coeff. μ	0.6
Rolling Friction Coeff. μ_r	0.00
Restitution Coef. e	0.1
Poisson Ratio σ	0.45
Young’s Modulus E (MPa)	5
Density ρ_p (kg/m ³)	2500

219 The first step was to simulate a pure fluid (in the absence of solid particles) flow-
 220 ing in the periodic channel until reaching fully-developed turbulence, and store the out-
 221 put to be used as initial condition in the CFD-DEM simulations (which are periodic only
 222 for the fluid). This step aimed at obtaining the initial conditions for the fluid with rel-
 223 atively low computational cost. Then, prior to each simulation, the grains are allowed
 224 to fall freely in stationary water, forming a conical heap in the channel center. Finally,
 225 the CFD-DEM simulations begin by imposing a turbulent water flow (whose initial con-
 226 dition was the previously stored fully-turbulent flow), which deforms the conical pile into
 227 a barchan dune. When a developed barchan is achieved, the flow is stopped and its di-
 228 rection reversed. Files with the setups used in our CFD-DEM simulations are available
 229 in an open repository (Assis et al., 2023).

230 4 Results and Discussion

231 4.1 Development of a dune from an initial heap

232 For the experiments outlined in cases *a* to *f* (Table 1), we followed the bedform
 233 as it evolves from an initial heap into a 2D dune. For example, Figure 2 shows recon-
 234 structed snapshots of an initial pile being deformed into a 2D dune for case *c*. We ini-
 235 tially observe the elongation of the upstream side and the formation of an avalanche face
 236 downstream of the crest, with the corresponding decrease of the crest height. Afterward,
 237 from a certain time on (76 s in this case), the dune keeps roughly the same shape, in-
 238 dicating a developed state. On the right, Figure 2 shows the superposition of the side
 239 view of the initial ($t = 4$ s, in darker gray) and developed ($t = 76$ s, in lighter gray) dunes.
 240 Because the intersected area (in black) is proportional to the number of grains that did
 241 not move (not necessarily equal, though), it indicates that a considerable part of the dune
 242 remains static, and that the dune reaches its developed form prior to a complete turnover.

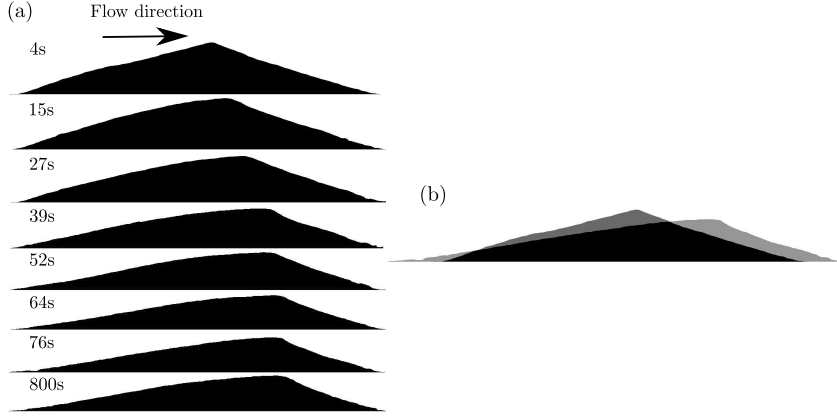


Figure 2. (a) Snapshots showing lateral-view images of an initial heap being deformed into a 2D dune for case *c* (Table 1). The flow is from left to right in the images, and the corresponding time instants are shown on the left. (b) Superposition of the side view of the initial ($t = 4$ s, in darker gray) and developed ($t = 76$ s, in lighter gray) bedforms (intersection appears in black).

243 In order to investigate further the dune development, we measured the main morpho-
 244 logical scales (length L , height Z and slope θ) along time.

245 Figures 3a–f present the vertical position of the maximum height (crest) of bed-
 246 forms, Z , as a function of time, t , for cases *a* to *f*, respectively. In this figure, Z is nor-
 247 malized by the dune length in the streamwise direction, L , and time t_c which is a timescale
 248 for the growth of subaqueous barchans proposed by Alvarez and Franklin (2017),

$$t_c = \frac{L_{eq}(\rho_p/\rho)(\rho_p/\rho - 1)gd}{(u_*^2 - u_{th}^2)^{3/2}}, \quad (5)$$

249 where u_{th} is shear velocity at the threshold for the incipient motion of grains, L_{eq} is the
 250 length of the developed dune, and $g = |\vec{g}|$. Because t_c in Equation 5 is proportional to
 251 L_{eq} divided by the dune celerity (displacement velocity of the dune crest), it scales with
 252 the dune turnover time. In Equation 5, we computed the threshold velocity in accordance
 253 with Andreotti et al. (2002).

254 For all cases, we observe in Figure 3 the existence of two timescales: a fast timescale
 255 occurring for $t/t_c < 5$, where Z/L decreases relatively fast, and a slow one for $t/t_c > 10$,
 256 where Z/L remains constant or oscillates around a mean value (plateau). While the fast
 257 timescale represents the flattening of the initial heap being deformed into a dune, the
 258 slow timescale indicates the presence of a developed dune. Therefore, the intersection
 259 between those two scales corresponds to the typical time for the formation of a 2D dune
 260 from an initial heap, for which we find $t/t_c \approx 5$. This value is higher, but of the same
 261 order of magnitude, of that found by Alvarez and Franklin (2017) for the development
 262 of barchan dunes based on the growth of their horns: $t/t_c \approx 2.5$. Because the mecha-
 263 nisms of barchan formation are different from those of 2D dunes, which do not have horns,
 264 this proximity of typical times is a strong indication of the existence of a similitude be-
 265 tween the 2D dunes and the central slice of barchans. In order to inquire further into
 266 it, we performed three-dimensional CFD-DEM simulations of an initial pile being de-
 267 formed into a barchan dune by a water flow, and analyze next the behavior of its cen-
 268 tral slice. Figure 4 shows snapshots of the central slice of a barchan dune (width equal
 269 to 2 mm, i.e., $10d$ for different instants (see the supporting information for snapshots show-
 270 ing top view images of the barchan dune, and a movie showing the time evolution of the

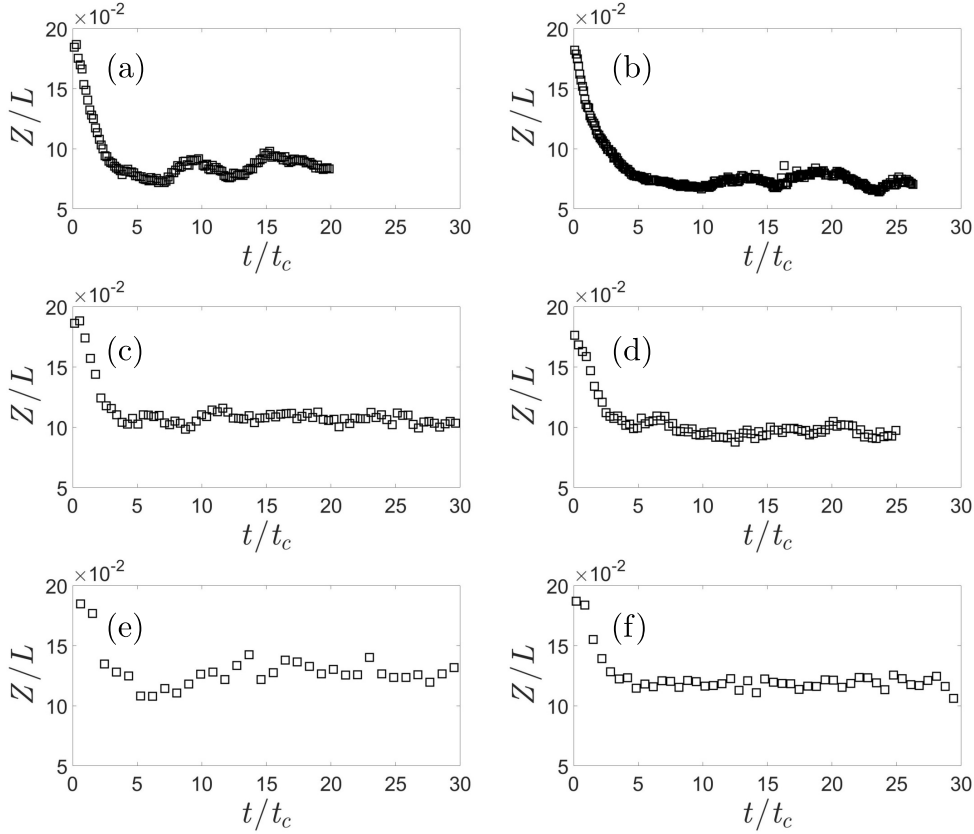


Figure 3. Vertical position of the maximum height (crest) of bedforms Z normalized by the dune length L , as a function of time t normalized by the timescale t_c . Figures (a), (c), (e) and (b), (d), (f) correspond to cases d , e , f and a , b , c (Table 1), respectively.

271 central slice). This width was chosen to avoid excessive fluctuations (due to the lack of
 272 grains in the spanwise direction) while analyzing the central slice only. Figures show-
 273 ing the longitudinal distribution of the slope, $\theta(x)$, for different time instants are avail-
 274 able in the supporting information, for both the experiments and numerical simulations
 275 (central slice). They present a similar trend, with slightly higher mean values of $\theta(x)$ for
 276 the experiment.

277 In our simulations, the central slice had a much smaller number of grains than the
 278 2D dunes, which was imposed by the computational costs of the CFD-DEM simulations
 279 (we limited the total number of grains in order to keep simulation times small). Even
 280 with this size difference, we observe that Figure 4 shows a behavior similar to that of Fig-
 281 ure 2, with an elongation of the upstream side and formation of an avalanche face on the
 282 lee side, until a stable shape is reached (after 85 s. See figure S10 in the supporting in-
 283 formation for the superposition of the central slice of the numerical dune). Figure 5a shows
 284 the time evolution of the horn length L_h , normalized by the characteristic length L_{drag} ,
 285 as the conical pile is deformed into a barchan dune. In Figures 5a and 5b, L_h is com-
 286 puted as the average of the two horns, and $L_{drag} = (\rho_p/\rho_f)d$ is an inertial length, pro-
 287 portional to the flux saturation length (Hersen et al., 2002). We observe an increase in
 288 L_h along time, until a plateau is reached at $t/t_c \approx 1-1.5$, with L_h oscillating around a
 289 mean value. The origin of oscillations are probably the small number of particles and

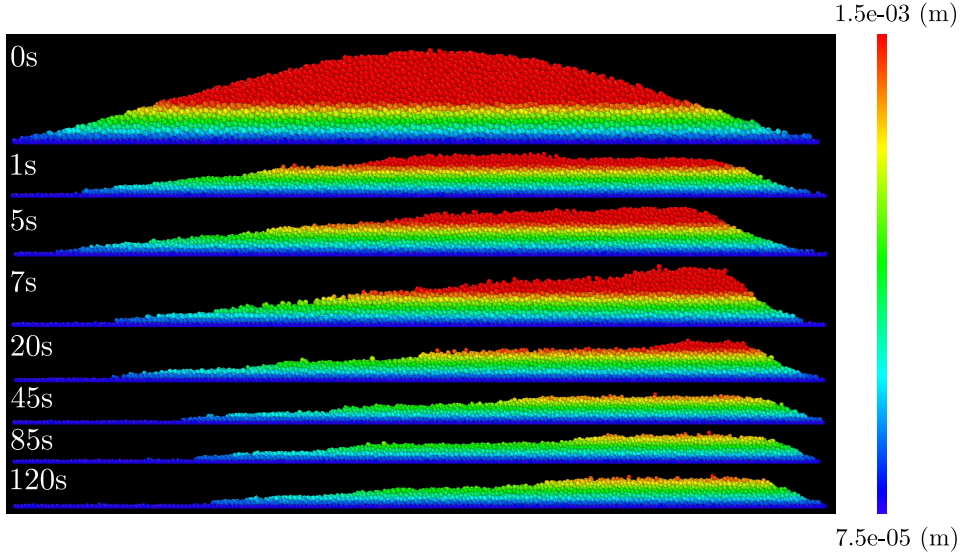


Figure 4. Snapshots showing the central slice of a bedform being deformed into a barchan dune. The water flow is from left to right and the color represents the height (scale in the color bar on the right). The corresponding time instants are shown on the left.

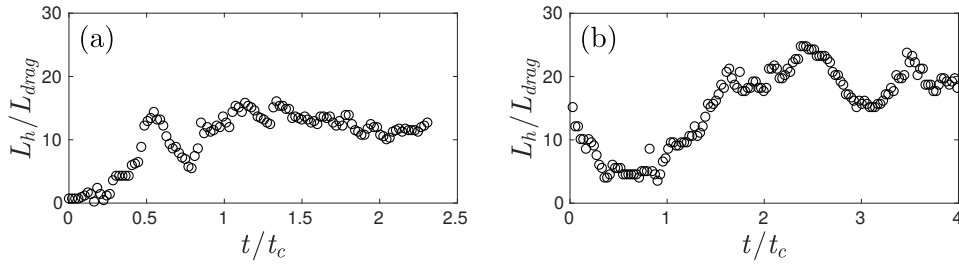


Figure 5. Time evolution of the horn length L_{horn} normalized by the characteristic length L_{drag} for (a) a barchan developed from a conical pile, and (b) for a barchan undergoing flow reversal. Results from numerical simulations, and the time is normalized by t_c .

290 the intermittent motion of grains. For this very small barchan, the time to reach the plateau
 291 is of the same order as that obtained experimentally by Alvarez and Franklin (2017).

292 In summary, by comparing the formation of 2D dunes with that of barchans from
 293 an initial heap (triangular in two and conical in three dimensions), we observe a certain
 294 similarity between them, the central slice of the barchan dune behaving roughly as a 2D
 295 dune.

296 4.2 Flow reversal

297 We inquire now into the process of inverting a dune by reversing the water flow.
 298 To create this condition, we performed experiments and numerical simulations in which
 299 we reversed the water flow after assuring that the dune was in a steady-state developed
 300 state. For the experiments with 2D dunes, this corresponds to cases *g* to *l* of Table 1.
 301 Figure 6 shows reconstructed snapshots of an initially developed 2D dune undergoing
 302 a flow reversal (case *h*). We notice that initially the motion occurs over the previous avalanche

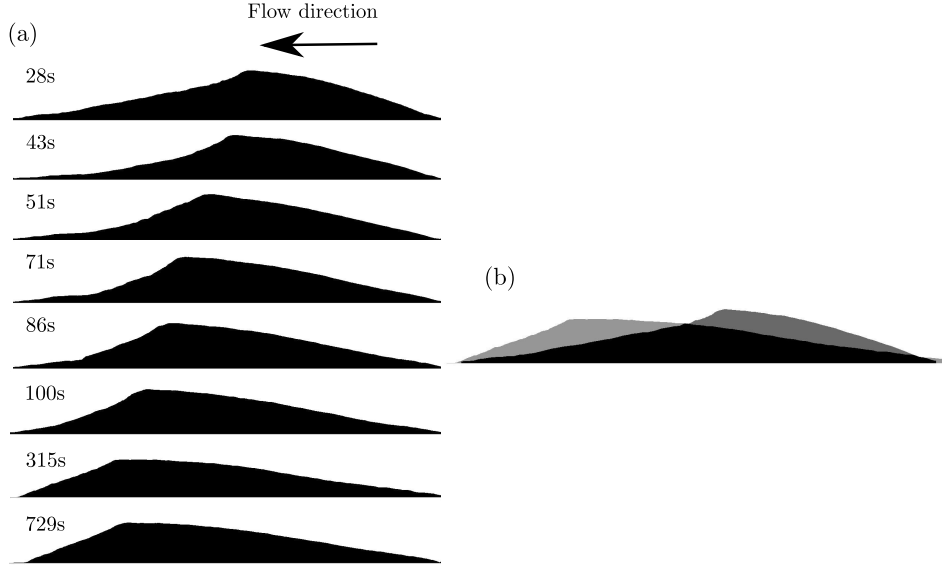


Figure 6. (a) Snapshots showing lateral-view images of an initially developed 2D dune undergoing a flow reversal for case *h* (Table 1). The flow is from right to left in the images, and the corresponding time instants are shown on the left (time set to 0 s at the beginning of the reversed flow). (b) Superposition of the side view of the initial ($t = 28$ s, in darker gray) and developed ($t = 315$ s, in lighter gray) bedforms (intersection appears in black).

303 face, which has its slope decreased over time while the crest is displaced to the left. At
 304 the same time, a new lee face develops over the previous stoss side, with the crest and
 305 a small avalanche face migrating over it. During this process (within 28 s and 100 s in
 306 Figure 6), the new lee face has a varying angle, going from the avalanche angle (near the
 307 crest) to a very low slope (close to the new trailing edge). When the avalanche face reaches
 308 the trailing edge, the dune is properly inverted. In order to investigate further the re-
 309 versal process, we measured the main morphological scales, which we present next.

310 Figures 7a–f show the vertical position of the maximum height (crest) of bedforms,
 311 Z/L , as a function of time, t/t_c , for cases *g* to *l*, respectively. If we neglect the small ini-
 312 tial rise in Figures 7a–c and 7f, we observe basically the existence of three timescales:
 313 (i) a fast timescale occurring for $t/t_c < 5$, for which Z decreases over time, represent-
 314 ing the initial flattening of the dune. During the flattening, the crest region diffuses and
 315 moves downstream, and the former avalanche face moves over the former stoss slope (be-
 316 tween 28 s and 71s in Figure 6); (ii) a fast timescale occurring within $5 < t/t_c < 10$, for
 317 which Z increases over time. This is due to the formation of a new avalanche face over
 318 the former stoss side while the crest continues its downstream motion; and (iii) a slow
 319 timescale for $t/t_c > 10$, where Z/L remains constant or oscillates around a mean value,
 320 indicating a developed form. Therefore, the total time for achieving an inverted dune
 321 is $t/t_c \approx 10$, approximately twice that for development from an initial heap.

322 Following a similar procedure as for the barchan formation, we carried out CFD-
 323 DEM simulations of a barchan undergoing inversion, and analyzed the behavior of its
 324 central slice. For that, we started with the developed barchan obtained in previous sim-
 325 ulations and reversed the flow direction. Figure 8 shows snapshots of the central slice
 326 of a barchan undergoing inversion for different instants (see the supporting information
 327 for snapshots showing top view images of the barchan dune, and a movie showing the
 328 central slice during the inversion). Although the central slice has a much smaller num-

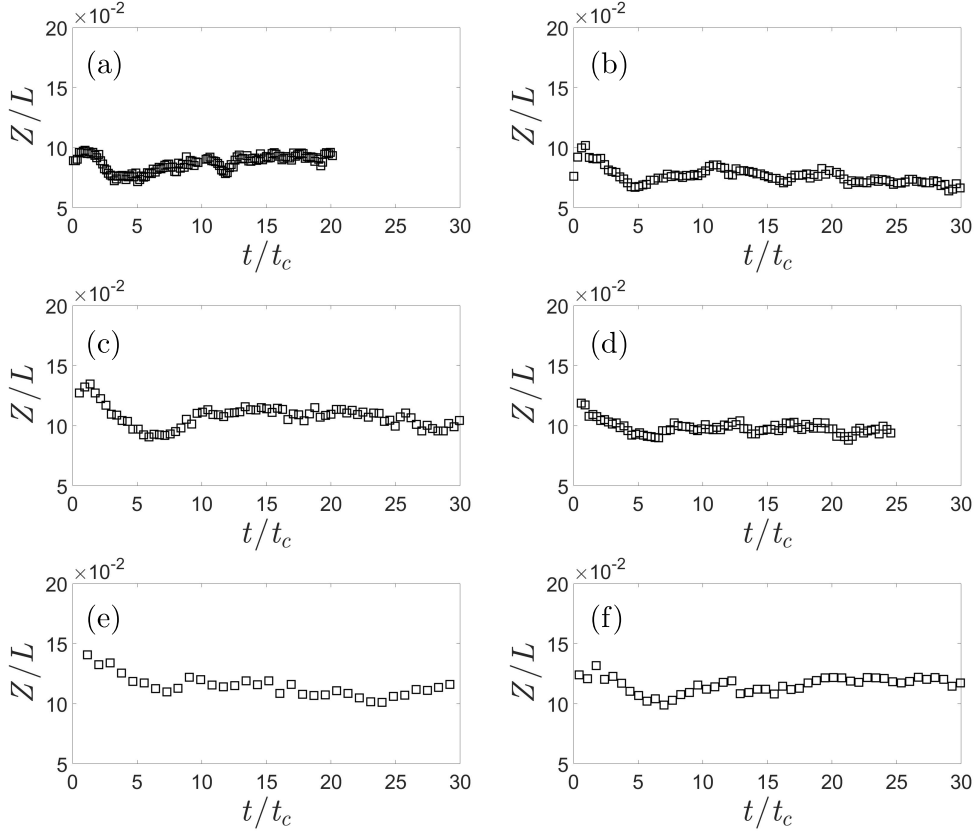


Figure 7. Vertical position of the maximum height (crest) of bedforms Z normalized by the dune length L , as a function of time t normalized by the timescale t_c . Figures (a), (c), (e) and (b), (d), (f) correspond to cases j , k , l and g , h , i (Table 1), respectively. Figures (a) to (f) correspond to cases g to l (Table 1), respectively.

329 ber of grains than the 2D dune, we observe a certain similarity between them: the crest
 330 and former avalanche face move over the former stoss side, and the latter becomes the
 331 new lee side. During the inversion process, the new lee side has a varying slope that goes
 332 from a very low angle (close to the new trailing edge, former toe) to an avalanche angle
 333 (just downstream the crest). Figures showing $\theta(x)$ at different time instants for the
 334 reversing dune are available in the supporting information, for both the experiments and
 335 numerical simulations (central slice). Here, they also present a similar trend, with slightly
 336 higher mean values of $\theta(x)$ for the experiment.

337 In order to identify the time to attain a developed barchan, we proceeded as in Alvarez
 338 and Franklin (2017) and tracked the growth of horns. Figure 5b shows the time evolu-
 339 tion of the horn length L_h , normalized by the characteristic length L_{drag} , for a barchan
 340 undergoing reversal. We observe that initially the existing horns shrink (L_h decreases),
 341 disappearing completely when $t/t_c \approx 1$, and from this time on the new horns begin to
 342 develop (L_h increases). When $t/t_c \approx 2-2.5$, the new horns seem to reach a developed state
 343 (L_h reaches a plateau, oscillating around a mean value). Therefore, the barchan, as the
 344 2D dune, takes twice the time to be completely inverted when compared with the forma-
 345 tion from an initially conical heap.

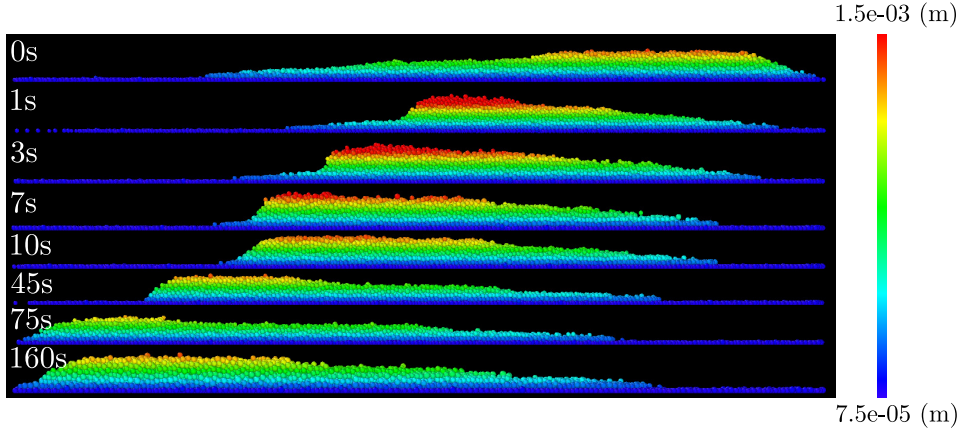


Figure 8. Snapshots showing the central slice of a barchan dune undergoing a flow reversal. The water flow is from right to left, and the color represents the height (scale in the colorbar on the right). The corresponding time instants are shown on the left.

346

4.3 Development vs reversal: t_c and mobility of grains

347

348

349

350

351

352

In the previous subsections, we compared 2D dunes with the central slice of 3D barchans. We found that the characteristic time for the development of 2D dunes is $5 t_c$, where t_c is a timescale used for the growth of barchan dunes. We also showed that for both 2D and barchan dunes the characteristic time to completely invert the dune under a flow reversal is twice that for the dune formation. These are relevant results indicating that the central slice of a barchan dune behaves roughly as a 2D dune.

353

354

355

356

357

358

359

360

361

We now investigate the mobility of grains during the development and inversion of dunes. Since the numerical simulations compute the instantaneous position of each grain, we can track the motion of all grains as a function of time. Therefore, we measured the mobility of grains in the central slice during the barchan development and inversion. For example, Figure 9 shows in red the grains with instantaneous velocities greater than $0.1u_*$ (typical bedload velocity over the dune, Wenzel & Franklin, 2019). We observe that only a few grains are mobilized within the central slice at each instant: only grains close to the surface move as bedload and grain below the surface remain static until exposed.

362

363

364

365

366

367

368

369

In order to know the proportion of moving grains with respect to the total, we counted the number of grains in the central slice that moved as bedload until a developed state was reached. We obtained that approximately 23% of grains remained static during the development from the initial heap and 20% of grains remained static during the barchan reversal. We conclude that 1/5th of the grains in the central slice remain static when a dune develops from a different bedform. A description of the procedure for identifying and counting the moving grains and a table listing the instantaneous number of grains moving as bedload at each instant are available in the supporting information.

370

371

372

373

Finally, we measured the number of grains lost by the barchan dune along time. In terms of rates, we observed that during inversion the dune loses 10–15% more grains than during its formation from a conical heap, as illustrated in the supporting information by tracing the amount of particles being lost over time.

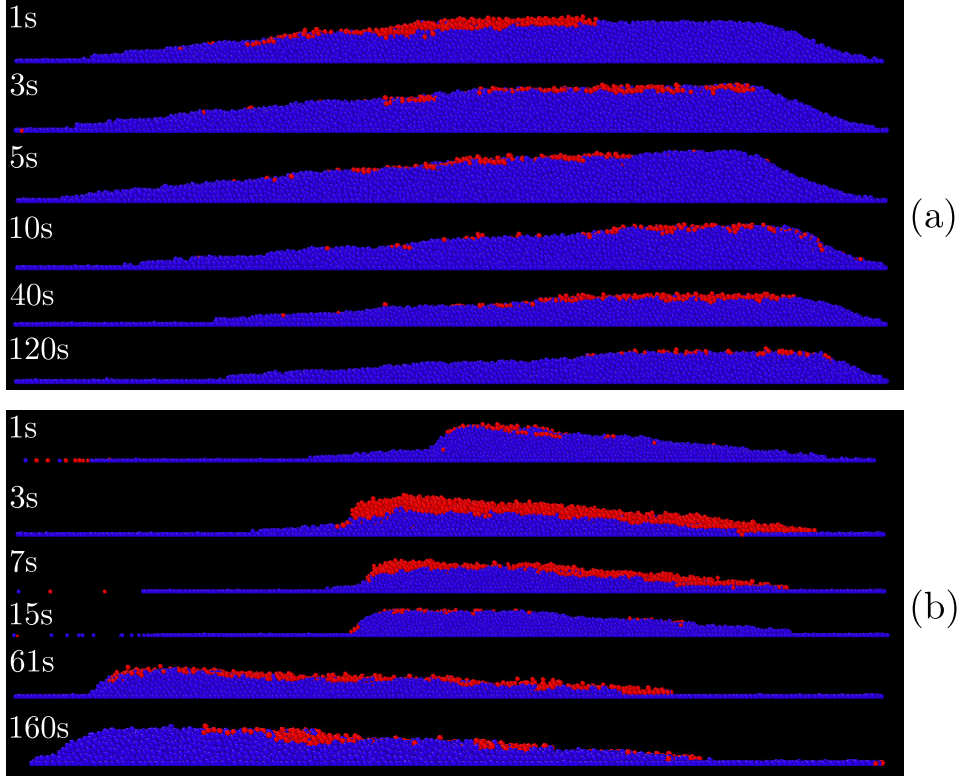


Figure 9. Snapshots showing grains being entrained as bedload (red particles) and static (blue) in the central slice of a barchan dune. (a) Development from an initial heap and (b) barchan undergoing a reversal. The corresponding time instants are shown on the left.

5 Conclusions

374

375 In this paper, we investigated the similarities between a real 2D dune and the central
 376 slice of a 3D barchan dune, and how these dunes react under flow reversals. For that,
 377 we carried out experiments in a 2D flume and CFD-DEM simulations of 3D dunes where
 378 an initial heap was deformed into a dune that, by reversing the flow, evolved afterward
 379 toward an inverted dune. We found that the characteristic time for the development of
 380 2D dunes is $5 t_c$, where t_c is a timescale used for the growth of barchan dunes. By comparing
 381 earlier work on 3D dunes, we concluded that the characteristic time-scale for 2D
 382 dunes is equivalent to that for 3D barchans. We showed that for both 2D and 3D barchan
 383 dunes the characteristic time to completely invert the dune under a flow reversal is twice
 384 that for the dune formation, and we revealed the morphodynamics of reversing dunes:
 385 the grains on the lee side climb back the dune while its internal part and toe remain static,
 386 forming a new lee face. During the inversion process, the new lee side has a varying slope
 387 that goes from a very small angle (close to the new trailing edge, former toe) to an avalanche
 388 angle (just downstream the crest). We also showed that a considerable part of grains (around
 389 20%) remain static during the entire process, and that the barchan dune loses more grains
 390 during the reversal than during its formation from a conical pile. Our findings reveal the
 391 mechanisms for dune reversal, and provide a proof-of-concept that, in some cases, numerical
 392 simulations of 3D barchans can be reduced to a central slice of a 2D dune, even
 393 in the subaqueous case.

Open Research

Data (digital images) supporting this work were generated by ourselves and are available in Mendeley Data (Assis et al., 2023) under the CC-BY-4.0 license. The numerical scripts used to process the images and the numerical setup for simulations are also available in Mendeley Data (Assis et al., 2023) under the CC-BY-4.0 license.

Acknowledgments

Willian Assis and Erick Franklin are grateful to the São Paulo Research Foundation – FAPESP (Grant Nos. 2018/14981-7, 2019/10239-7 and 2021/12910-8) and Conselho Nacional de Desenvolvimento Científico e Tecnológico – CNPq (Grant No. 405512/2022-8) for the financial support provided. N. M. Vriend is supported by a Royal Society University Research Fellowship No. URF/R1/191332. Willian Assis would like to express his gratitude to Karol Bacik and Nicolao Lima for their assistance in the experimental and numerical parts of this research, respectively.

References

- Alvarez, C. A., & Franklin, E. M. (2017, Dec). Birth of a subaqueous barchan dune. *Phys. Rev. E*, *96*, 062906. Retrieved from <https://link.aps.org/doi/10.1103/PhysRevE.96.062906> doi: 10.1103/PhysRevE.96.062906
- Alvarez, C. A., & Franklin, E. M. (2018, Oct). Role of transverse displacements in the formation of subaqueous barchan dunes. *Phys. Rev. Lett.*, *121*, 164503. Retrieved from <https://link.aps.org/doi/10.1103/PhysRevLett.121.164503> doi: 10.1103/PhysRevLett.121.164503
- Alvarez, C. A., & Franklin, E. M. (2019, Oct). Horns of subaqueous barchan dunes: A study at the grain scale. *Phys. Rev. E*, *100*, 042904. Retrieved from <https://link.aps.org/doi/10.1103/PhysRevE.100.042904> doi: 10.1103/PhysRevE.100.042904
- Alvarez, C. A., & Franklin, E. M. (2020, Jan). Shape evolution of numerically obtained subaqueous barchan dunes. *Phys. Rev. E*, *101*, 012905. Retrieved from <https://link.aps.org/doi/10.1103/PhysRevE.101.012905> doi: 10.1103/PhysRevE.101.012905
- Alvarez, C. A., & Franklin, E. M. (2021). Force distribution within a barchan dune. *Phys. Fluids*, *33*(1), 013313.
- Andreotti, B., Claudin, P., & Douady, S. (2002). Selection of dune shapes and velocities. part 1: Dynamics of sand, wind and barchans. *Eur. Phys. J. B*, *28*, 321-329.
- Andreotti, B., Fourrière, A., Ould-Kaddour, F., Murray, B., & Claudin, P. (2009). Giant aeolian dune size determined by the average depth of the atmospheric boundary layer. *Nature*, *457*, 1120-1123.
- Assis, W. R., & Franklin, E. M. (2020). A comprehensive picture for binary interactions of subaqueous barchans. *Geophys. Res. Lett.*, *47*(18), e2020GL089464.
- Assis, W. R., & Franklin, E. M. (2021). Morphodynamics of barchan-barchan interactions investigated at the grain scale. *J. Geophys. Res.: Earth Surf.*, *126*(8), e2021JF006237.
- Assis, W. R., Franklin, E. M., & Vriend, N. M. (2023). Dataset for “evolving dunes under flow reversals: from an initial heap toward inverted dune” [Dataset][Software]. *Mendeley Data*, <http://dx.doi.org/10.17632/fw3bcrxknf.1> doi: 10.17632/fw3bcrxknf.1
- Bacik, K. A., Canizares, P., Caulfield, C.-c. P., Williams, M. J., & Vriend, N. M. (2021, Oct). Dynamics of migrating sand dunes interacting with obstacles. *Phys. Rev. Fluids*, *6*, 104308. Retrieved from <https://link.aps.org/doi/10.1103/PhysRevFluids.6.104308> doi: 10.1103/PhysRevFluids.6.104308

- 444 Bacik, K. A., Caulfield, C.-c. P., & Vriend, N. M. (2021, Oct). Stability of the
 445 interaction between two sand dunes in an idealized laboratory experiment.
 446 *Phys. Rev. Lett.*, *127*, 154501. Retrieved from [https://link.aps.org/doi/](https://link.aps.org/doi/10.1103/PhysRevLett.127.154501)
 447 [10.1103/PhysRevLett.127.154501](https://link.aps.org/doi/10.1103/PhysRevLett.127.154501) doi: 10.1103/PhysRevLett.127.154501
- 448 Bacik, K. A., Lovett, S., Caulfield, C.-c. P., & Vriend, N. M. (2020, Feb). Wake
 449 induced long range repulsion of aqueous dunes. *Phys. Rev. Lett.*, *124*, 054501.
 450 Retrieved from [https://link.aps.org/doi/10.1103/PhysRevLett.124](https://link.aps.org/doi/10.1103/PhysRevLett.124.054501)
 451 [.054501](https://link.aps.org/doi/10.1103/PhysRevLett.124.054501) doi: 10.1103/PhysRevLett.124.054501
- 452 Bagnold, R. A. (1941). *The physics of blown sand and desert dunes*. London: Chap-
 453 man and Hall.
- 454 Berger, R., Kloss, C., Kohlmeyer, A., & Pirker, S. (2015). Hybrid parallelization of
 455 the LIGGGHTS open-source DEM code. *Powder Technology*, *278*, 234-247.
- 456 Claudin, P., & Andreotti, B. (2006). A scaling law for aeolian dunes on Mars,
 457 Venus, Earth, and for subaqueous ripples. *Earth Plan. Sci. Lett.*, *252*, 20-44.
- 458 Courrech du Pont, S. (2015). Dune morphodynamics. *C. R. Phys.*, *16*(1), 118 - 138.
- 459 Elbelrhiti, H., Claudin, P., & Andreotti, B. (2005). Field evidence for surface-wave-
 460 induced instability of sand dunes. *Nature*, *437*(04058).
- 461 Franklin, E. M., & Charru, F. (2011). Subaqueous barchan dunes in turbulent shear
 462 flow. Part 1. Dune motion. *J. Fluid Mech.*, *675*, 199-222.
- 463 Goniva, C., Kloss, C., Deen, N. G., Kuipers, J. A. M., & Pirker, S. (2012). Influence
 464 of rolling friction on single spout fluidized bed simulation. *Particuology*, *10*(5),
 465 582-591.
- 466 Guignier, L., Niiya, H., Nishimori, H., Lague, D., & Valance, A. (2013, May).
 467 Sand dunes as migrating strings. *Phys. Rev. E*, *87*, 052206. Retrieved
 468 from <https://link.aps.org/doi/10.1103/PhysRevE.87.052206> doi:
 469 [10.1103/PhysRevE.87.052206](https://link.aps.org/doi/10.1103/PhysRevE.87.052206)
- 470 Herrmann, H. J., & Sauer mann, G. (2000). The shape of dunes. *Physica A (Amster-*
 471 *dam)*, *283*, 24-30.
- 472 Hersen, P. (2004). On the crescentic shape of barchan dunes. *Eur. Phys. J. B*,
 473 *37*(4), 507-514.
- 474 Hersen, P., Andersen, K. H., Elbelrhiti, H., Andreotti, B., Claudin, P., & Douady,
 475 S. (2004, Jan). Corridors of barchan dunes: Stability and size selection. *Phys.*
 476 *Rev. E*, *69*, 011304. Retrieved from [https://link.aps.org/doi/10.1103/](https://link.aps.org/doi/10.1103/PhysRevE.69.011304)
 477 [PhysRevE.69.011304](https://link.aps.org/doi/10.1103/PhysRevE.69.011304) doi: 10.1103/PhysRevE.69.011304
- 478 Hersen, P., Douady, S., & Andreotti, B. (2002, Dec). Relevant length
 479 scale of barchan dunes. *Phys. Rev. Lett.*, *89*, 264301. Retrieved from
 480 <https://link.aps.org/doi/10.1103/PhysRevLett.89.264301> doi:
 481 [10.1103/PhysRevLett.89.264301](https://link.aps.org/doi/10.1103/PhysRevLett.89.264301)
- 482 Jarvis, P., Bacik, K., Narteau, C., & Vriend, N. (2022). Coarsening dynamics of
 483 2d subaqueous dunes. *Journal of Geophysical Research: Earth Surface*, *127*(2),
 484 e2021JF006492.
- 485 Khosronejad, A., & Sotiropoulos, F. (2017). On the genesis and evolution of barchan
 486 dunes: morphodynamics. *J. Fluid Mech.*, *815*, 117-148.
- 487 Kidanemariam, A. G., & Uhlmann, M. (2014). Direct numerical simulation of pat-
 488 tern formation in subaqueous sediment. *J. Fluid Mech.*, *750*, R2.
- 489 Kloss, C., & Goniva, C. (2010). LIGGGHTS: a new open source discrete element
 490 simulation software. In *Proc. 5th int. conf. on discrete element methods*. Lon-
 491 don, UK.
- 492 Kroy, K., Fischer, S., & Obermayer, B. (2005). The shape of barchan dunes. *J.*
 493 *Phys. Condens. Matter*, *17*, S1229-0S1235.
- 494 Kroy, K., Sauer mann, G., & Herrmann, H. J. (2002a, Sep). Minimal model for ae-
 495 lian sand dunes. *Phys. Rev. E*, *66*, 031302. Retrieved from [https://link.aps](https://link.aps.org/doi/10.1103/PhysRevE.66.031302)
 496 [.org/doi/10.1103/PhysRevE.66.031302](https://link.aps.org/doi/10.1103/PhysRevE.66.031302) doi: 10.1103/PhysRevE.66.031302
- 497 Kroy, K., Sauer mann, G., & Herrmann, H. J. (2002b, Jan). Minimal model for sand
 498 dunes. *Phys. Rev. Lett.*, *88*, 054301. Retrieved from <https://link.aps.org/>

- doi/10.1103/PhysRevLett.88.054301 doi: 10.1103/PhysRevLett.88.054301
- 499 Lima, N. C., Assis, W. R., Alvarez, C. A., & Franklin, E. M. (2022). Grain-scale
500 computations of barchan dunes. *Phys. Fluids*, *34*(12), 123320. Retrieved from
501 <https://doi.org/10.1063/5.0121810> doi: 10.1063/5.0121810
- 502 Pähitz, T., Kok, J. F., Parteli, E. J. R., & Herrmann, H. J. (2013). Flux saturation
503 length of sediment transport. *Phys. Rev. Lett.*, *111*, 218002.
- 504 Parteli, E. J. R., Andrade, J. S., & Herrmann, H. J. (2011, Oct). Transverse insta-
505 bility of dunes. *Phys. Rev. Lett.*, *107*, 188001. Retrieved from [https://link](https://link.aps.org/doi/10.1103/PhysRevLett.107.188001)
506 [.aps.org/doi/10.1103/PhysRevLett.107.188001](https://link.aps.org/doi/10.1103/PhysRevLett.107.188001) doi: 10.1103/PhysRevLett
507 [.107.188001](https://link.aps.org/doi/10.1103/PhysRevLett.107.188001)
- 508
- 509 Parteli, E. J. R., Durán, O., Bourke, M. C., Tsoar, H., Pöschel, T., & Herrmann,
510 H. (2014). Origins of barchan dune asymmetry: Insights from numerical
511 simulations. *Aeol. Res.*, *12*, 121-133.
- 512 Parteli, E. J. R., Durán, O., & Herrmann, H. J. (2007, Jan). Minimal size of a
513 barchan dune. *Phys. Rev. E*, *75*, 011301. Retrieved from [https://link.aps](https://link.aps.org/doi/10.1103/PhysRevE.75.011301)
514 [.org/doi/10.1103/PhysRevE.75.011301](https://link.aps.org/doi/10.1103/PhysRevE.75.011301) doi: 10.1103/PhysRevE.75.011301
- 515 Parteli, E. J. R., & Herrmann, H. J. (2007, Oct). Dune formation on the present
516 mars. *Phys. Rev. E*, *76*, 041307. Retrieved from [https://link.aps.org/doi/](https://link.aps.org/doi/10.1103/PhysRevE.76.041307)
517 [10.1103/PhysRevE.76.041307](https://link.aps.org/doi/10.1103/PhysRevE.76.041307) doi: 10.1103/PhysRevE.76.041307
- 518 Sauermann, C., Rognon, P., Poliakov, A., & Herrmann, H. J. (2000). The shape of
519 the barchan dunes of Southern Morocco. *Geomorphology*, *36*, 47-62.
- 520 Sauermann, G., Kroy, K., & Herrmann, H. J. (2001, Aug). Continuum saltation
521 model for sand dunes. *Phys. Rev. E*, *64*, 031305. Retrieved from [https://](https://link.aps.org/doi/10.1103/PhysRevE.64.031305)
522 link.aps.org/doi/10.1103/PhysRevE.64.031305 doi: 10.1103/PhysRevE
523 [.64.031305](https://link.aps.org/doi/10.1103/PhysRevE.64.031305)
- 524 Schwämmle, V., & Herrmann, H. J. (2005). A model of barchan dunes including lat-
525 eral shear stress. *Eur. Phys. J. E*, *16*(1), 57-65.
- 526 Wenzel, J. L., & Franklin, E. M. (2019). Velocity fields and particle trajectories for
527 bed load over subaqueous barchan dunes. *Granular Matter*, *21*, 321-334.
- 528 Zhang, D., Yang, X., Rozier, O., & Narteau, C. (2014). Mean sediment residence
529 time in barchan dunes. *J. Geophys. Res.: Earth Surf.*, *119*(3), 451-463.